How do Cl concentrations matter for simulating CH_4, $\delta^{13}C(CH_4)$ and estimating CH_4 budget through atmospheric inversions ? - Supplementary Material

Joël Thanwerdas[1,*], Marielle Saunois[1], Antoine Berchet[1], Isabelle Pison[1], and Philippe Bousquet[1]

[1]Laboratoire des Sciences du Climat et de l'Environnement, CEA-CNRS-UVSQ, IPSL, Gif-sur-Yvette, France.

Correspondence: J. Thanwerdas (joel.thanwerdas@lsce.ipsl.fr)

The Supplementary Material provides additional information about fluxes and source isotopic signatures prescribed in the multiple sensitivity simulations (Text S1, Figure S1, Figure S2, Figure S3, Table S1, Table S2 and Table S3). Also, a demonstration of the value used by an inversion system to adjust the globally-averaged source isotopic signature and reduce the mean isotopic signal bias is provided (Text S2). In addition, Tables S5 and S6 provide a list of CH_4 and $\delta^{13}C(CH_4)$ surface stations used in this study. Table S4 and Figure S4 provide the locations and a list of AirCore profiles. Finally, Text S3 and Figure S5 provide an analysis of the influence of Cl concentrations on XCH_4.

1 Text S1 : Optimized CH_4 fluxes and $\delta^{13}C(CH_4)$ source isotopic signatures

1.1 Introduction

In this study, the system designed by Thanwerdas et al. (2021) is used to perform an inversion. The posterior CH_4 surface fluxes and $\delta^{13}C(CH_4)$ source isotopic signatures inferred by the inversion system are then used in the reference simulation (SimREF). This inversion aims to bring the simulated CH_4 and $\delta^{13}C(CH_4)$ values closer to the available observations and give more credibility to the conclusions of the paper.

The system of Thanwerdas et al. (2021) uses the variational approach that minimizes a cost function (Eq. 1) until a convergence criteria is reached:

$$J(\mathbf{x}) = \frac{1}{2}(\mathbf{x}-\mathbf{x}^{\mathrm{b}})^{\mathrm{T}}\mathbf{B}^{-1}(\mathbf{x}-\mathbf{x}^{\mathrm{b}}) + \frac{1}{2}(\mathscr{H}(\mathbf{x})-\mathbf{y}^{\mathrm{o}})^{T}\mathbf{R}^{-1}(\mathscr{H}(\mathbf{x})-\mathbf{y}^{\mathrm{o}}) \tag{1}$$

Here, $\mathbf{x}$ is the control vector including the variables optimized by the system. $\mathbf{x}^{\mathrm{b}}$ is the prior control vector including prior estimates of the control variables (i.e., before the inversion). $\mathbf{y}^{\mathrm{o}}$ is the observation vector that encompasses all observational data. $\mathbf{R}$ and $\mathbf{B}$ are the error covariance matrices associated with the observation errors and the prior errors, respectively. $\mathscr{H}$ is the observation operator that links the observation and control spaces.

Minimization is performed using the M1QN3 minimization algorithm (Gilbert and Lemaréchal, 1989). At each iteration, the gradient of the cost function at point $\mathbf{x}$ is calculated using Eq. 2.

$$\nabla J_{\mathbf{x}} = \mathbf{B}^{-1}(\mathbf{x}-\mathbf{x}^{\mathrm{b}}) + \mathscr{H}^{*}(\mathbf{R}^{-1}(\mathscr{H}(\mathbf{x})-\mathbf{y}^{\mathrm{o}})) \tag{2}$$

In practice, an iteration consists of two steps: a direct simulation which allows to calculate the cost function and an adjoint simulation which allows to calculate the gradient of the cost function at a specific point. In this inversion, the control vector **x** includes, for five categories presented below, CH_4 surface fluxes and associated $\delta^{13}C(CH_4)$ source isotopic signatures at the pixel scale. Initial conditions are also included in **x**.

1.2 CH_4 fluxes

CH_4 surface fluxes are divided into five emission categories:

- Biofuels and Biomass burning sources (BB)
- Agriculture and Waste (AGW)
- Fossil Fuels and Geological sources (FFG)
- Oceanic and termite sources (NAT)
- Wetlands (WET)

We adopt the prior CH_4 emissions compiled for the inversions performed under the Global Methane Budget (Saunois et al., 2020). Anthropogenic emissions (including biofuels) and fire emissions are taken from the EDGARv432 (http://edgar.jrc.ec.europa.eu/overview.php?v=432&SECURE=123) and GFED4s (van der Werf et al., 2017) databases, respectively. Statistics from British Pretroleum (BP) and the Food and Agriculture Organization of the United Nations (FAO) are used to extend EDGARv432 emissions, which end in 2012, to 2017.

Estimates from natural sources are based on average values in the literature: Poulter et al. (2017) for wetlands, Kirschke et al. (2013) for termites, Lambert and Schmidt (1993) for oceanic sources and Etiope (2015) for geological sources. The soil sink is based on Ridgwell et al. (1999). CH_4 emissions are compiled in Table S1.

1.3 Source isotopic signatures

Each emission category is associated with a source isotopic signatures map in order to extract $^{12}CH_4$ and $^{13}CH_4$ emissions from CH_4 emissions. References and globally-averaged source signatures are compiled in Table S2. Signatures maps are shown in Figure S2.

1.4 Sinks

Concentrations of species that remove CH_4 from the atmosphere (OH, $O(^1D)$, Cl) are not included in the control vector **x** and therefore sink intensities are not optimized.

Three-dimensional and time-dependent oxidant concentration fields (OH, $O(^1D)$ and Cl) were simulated by the General Circulation Model LMDz coupled to the INCA [INteraction with Chemistry and Aerosols] chemistry model (Hauglustaine et al., 2021; Folberth et al., 2006; Hauglustaine et al., 2004). Seventeen ozone-depleting substances consisted of CFCs (CFC-12,

CFC-11, CFC-113), three HCFCs (HCFC-22, HCFC-141b, HCFC-142b), two halons (Halon-1211, Halon-1301), CH_3CCl_3, CCl_4, CH_3Cl, methylene chloride (CH_2Cl_2), chloroform ($CHCl_3$), methyl bromide (CH_3Br) and HFC-134a, and their associated photochemical reactions, were included in the INCA chemical scheme to produce Cl radicals (Terrenoire et al., 2020). In the LMDz-INCA simulations, surface concentrations of these long-lived Cl source species were prescribed based on historical data sets prepared by Meinshausen et al. (2017). The model was run for the period 1850-2018 (Hauglustaine et al., 2021).

This simulation was originally dedicated to the study of Cl in the stratosphere. To be consistent with our reference scenario, the tropospheric mean Cl concentration (330 molec.cm^{-3}) was scaled to that of Wang et al. (2019) (620 molec.cm^{-3}), very similar to that of Wang et al. (2021) (630 molec.cm^{-3})

Sink intensities over the period 1998-2018 and the associated fractionation coefficients are compiled in Table S3.

1.5 Assimilated observations

CH_4 observations between 1998 and 2018 provided by 79 surface stations of the Global Greenhouse Gas Reference Network (GGGRN), part of the NOAA-ESRL Global Monitoring Division (NOAA-ESRL GMD), are assimilated by the system (Table S5). In addition, flask samples retrieved at 22 NOAA-ESRL stations and analyzed by the Institute of Arctic and Alpine Research (INSTAAR) to provide $\delta^{13}C(CH_4)$ observations, are also assimilated (Table S6).

1.6 Model-observation agreement

As each iteration took 3 days to run, the inversion was stopped when a model-observation agreement sufficient to perform the analysis of the paper was obtained. The Root-Mean-Square Error (RMSE) on the global averages reach 3.6 ppb for CH_4 and 0.04 ‰ for $\delta^{13}C(CH_4)$ for SimREF (Figure S1).

2 Text S2 : Demonstration of the value of global source isotopic signature adjustment

Here, we demonstrate the result used in Sect. 3.3 of the main paper. That is, the bias of $\delta^{13}C(CH_4)$ between a sensitivity simulation and the SimREF simulation tends to a stabilized value (steady-state) that is equal to the adjustment value of the globally-averaged source isotopic signature applied by the inversion system. For ease of demonstration, this relationship is shown by approximating that the tropospheric mixing ratios of $^{12}CH_4$ are equal to those of CH_4 and we simplify the problem by reducing it to a one-box model problem.

If we start from a mass-conservation balance equation in a one-box problem, we have :

$$\begin{cases} \dfrac{dB}{dt} = S - k \cdot B \\ \dfrac{dB_{13}}{dt} = S_{13} - k_{13} \cdot B_{13} \end{cases} \tag{3}$$

where B et B_{13} are the total masses of $^{12}CH_4$ et $^{13}CH_4$ in the atmosphere, respectively. k and k_{13} are the reaction rate constants of $^{12}CH_4$ and $^{13}CH_4$ chemical sinks, respectively. S and S_{13} are the total sources of $^{12}CH_4$ and $^{13}CH_4$ (including soil sink as a negative source), respectively.

Let R_{atm}, R_s and $\varepsilon = \alpha - 1 = \frac{k_{13}}{k} - 1$ be the atmospheric isotopic ratio, the source isotopic ratio and the isotopic fractionation coefficient of the total chemical CH_4 sink. We can infer an equation linking these three terms :

$$\frac{dB_{13}}{dt} = S_{13} - k_{13} \cdot B_{13} \tag{4}$$

$$\implies \quad \frac{d(R_{\text{atm}} \cdot B)}{dt} = R_s \cdot S - (k \cdot \alpha) \cdot (R_{\text{atm}} \cdot B) \tag{5}$$

$$\implies \quad \frac{d(R_{\text{atm}} \cdot B)}{dt} = R_s \cdot S - (1+\varepsilon) \cdot R_{\text{atm}} \cdot P \tag{6}$$

At steady state, with time derivatives equal to zero, we have :

$$\begin{cases} S - P = 0 \\ R_s \cdot S - (1+\varepsilon) \cdot R_{\text{atm}} \cdot P = 0 \end{cases} \tag{7}$$

Subsequently, these equations can be reshaped to obtain a relationship between δ_a, which is the mean atmospheric isotopic signal at steady state, and δ_s, which is the globally-averaged source isotopic signature.

$$R_s \cdot S - (1+\varepsilon) \cdot R_{\text{atm}} \cdot P = 0 \tag{8}$$

$$\implies \quad R_s - (1+\varepsilon) \cdot R_{\text{atm}} = 0 \tag{9}$$

$$\implies \quad (1+\delta_s) \cdot R_{std} = (1+\varepsilon) \cdot (1+\delta_a) \cdot R_{std} \tag{10}$$

$$\implies \quad \delta_a = \frac{1+\delta_s}{1+\varepsilon} - 1 \tag{11}$$

With the isotopic signal being $\delta^{13}C(CH_4)$, we have $1+\varepsilon \approx 1$. To understand the effect of isotopic fractionation on the atmospheric isotopic signal, we choose to simplify the equation :

$$\delta_a \approx \delta_s - \varepsilon - \delta_s \cdot \varepsilon \approx \delta_s - \varepsilon \tag{12}$$

For CH_4, ε is negative, hence the isotopic fractionation of CH_4 sinks enriches the atmospheric isotopic signal in ^{13}C compared to the globally-averaged source isotopic signature.

We want to predict the adjustment value that an inversion system would apply to the source isotopic signature in order to increase the agreement between the simulated and observed mean atmospheric isotopic signal $\delta^{13}C(CH_4)$. To do so, we consider two simulations of CH_4 mole fractions and isotopic signal $\delta^{13}C(CH_4)$, denoted simulation n°1 and simulation n°2. We prescribe equal CH_4 sources with the same isotopic signature $\delta_{s,1} = \delta_{s,2}$. Also, we prescribe sinks with distinct fractionation coefficients ε_1 et ε_2. Equal initial conditions are adopted in the two simulations.

Little by little, a bias between the isotopic signals simulated by these two simulations will increase and stabilize after some decades :

$$\begin{cases} \delta_{a,1} \approx \delta_{s,1} - \varepsilon_1 - \delta_{s,1} \cdot \varepsilon_1 \\ \delta_{a,2} \approx \delta_{s,2} - \varepsilon_2 - \delta_{s,2} \cdot \varepsilon_2 \end{cases} \tag{13}$$

$$\implies \quad \Delta\delta_a \approx -\Delta\varepsilon \cdot (1 + \delta_{s,1}) \tag{14}$$

$$\implies \quad \Delta\varepsilon \approx -\frac{\Delta\delta_a}{1 + \delta_{s,1}} \tag{15}$$

We consider that $\delta_{a,1}$ represents the observed value and we decide to integrate the simulation n°2 into an inversion system to reduce the bias between $\delta_{a,2}$ and the observed value (here $\delta_{a,1}$). The inversion system will shift the source isotopic signature in order to remove this bias caused by the fractionation difference $\Delta\varepsilon$. The $\delta_{s,2}$ posterior value is denoted $\delta_{s,post}$. Using the Eq. 11, we can obtain the fractionation difference $\Delta\varepsilon$ between the two simulations from the bias $\Delta\delta_a$:

$$\begin{cases} \delta_{a,1} = \dfrac{1 + \delta_{s,1}}{1 + \varepsilon_1} - 1 \\ \delta_{a,2} = \delta_{a,1} = \dfrac{1 + \delta_{s,post}}{1 + \varepsilon_2} - 1 \end{cases} \tag{16}$$

$$\implies \quad \delta_{s,post} - \delta_{s,1} \approx -\Delta\varepsilon \cdot (1 + \delta_a) \tag{17}$$

Finally, we obtain the following relationship by combining the different equations :

$$\delta_{s,post} - \delta_{s,1} \approx -\Delta\delta_a \cdot \frac{1 + \delta_{a,1}}{1 + \delta_{s,1}} \approx -\Delta\delta_a \tag{18}$$

2.1 Text S3 : XCH_4 columns

We investigate the influence of Cl concentrations on column-averaged CH_4 dry-air mole fractions (hereafter referred to as simply XCH_4) using version 9.0 of the GOSAT Proxy XCH_4 dataset provided by the University of Leicester (Parker et al., 2020). The Greenhouse Gases Observing Satellite (GOSAT) carrying the Thermal And Near-infrared Sensor for carbon Observation Fourier Transport Spectrometer (TANSO-FTS) (Kuze et al., 2009) provides radiance measurements in a spectral band centered on a value close to 1.6 um, in which CH_4 has a high absorption capacity. The University of Leicester's retrieval algorithm is able to produce XCH_4 from these radiances. The dataset shows an accuracy of 13.72 ppb associated with a correlation coefficient of 0.92 when compared to the Total Carbon Column Observing Network (TCCON) data (Parker et al., 2020).

XCH_4 obtained by remote sensing techniques are now massively assimilated in inversions because satellite observations offer a much larger spatial coverage than in situ measurements. Ostler et al. (2016) showed that model errors in simulating stratospheric CH_4 contribute to model biases when compared to observed XCH_4 from TCCON. From our analysis of the CH_4 vertical profiles, we know that the biases generated by a modification of the Cl sink will likely affect the simulated XCH_4. To quantify the influence of the Cl field on XCH_4, vertical profiles simulated by LMDz-SACS are sampled at the observations locations and times in 2018 and convolved with the retrieval of a priori vertical profile and column averaging kernels provided by the University of Leicester. The individual XCH_4 retrievals and model simulations are aggregated in model-resolution grid boxes. We define the bias $b_{p,i}$ for a specific pixel p and a specific simulation i as :

$$b_{p,i} = \overline{\mathrm{X}_{p,i} - \mathrm{X}_{p,\mathrm{SimREF}}}^{p} \tag{19}$$

where $\mathrm{X}_{p,i}$ is a XCH_4 simulated value from the simulation i whose location is inside the pixel p. The mean bias is then an average over the whole year.

The mean biases exhibit a very small spatial variability (less than 1 ppb) for SimINCA, SimSherwen, SimNoTropo and SimTaki and are very close to the biases at the surface (difference of 6 ppb for SimTaki and 1-3 ppb for the others). For SimNoCl (see Fig. S5), those values are larger because the change in contribution from the stratospheric Cl sink between SimNoCl and SimREF (-1.1 %) is larger than between other simulations and SimREF ($+0.5$ % for SimTaki and ± 0.1 % for others). While the bias at the stations is about 20 ppb in 2018 for SimNoCl, those on the columns range from 20 ppb in the Tropics to 30 ppb in the higher latitudes. To summarize, if the Cl sink is removed, i) the bias becomes larger on the total column than at the surface and ii) the bias becomes latitude-dependent.

As in a surface-based inversion, a satellite-based inversion system would compensate for this bias by adjusting the surface fluxes. We cannot rigorously apply here the same methods as in Sect 3.2 of the main paper to calculate this adjustment because a box model representation is too simple to model the bias on XCH_4. Due to differences between XCH_4 and CH_4 biases, CH_4 global source adjustments inferred by a satellite-based inversion or by a surface-based inversion could be different. However, these biases differences are very small when the Cl stratospheric sink is modified within the realistic ranges given here and becomes noticeable only when the stratospheric Cl sink is neglected. We conclude that the results from the two types of inversions should be very similar when changing the Cl field.

Table S1. Prior and posterior estimates of global CH_4 emissions and associated flux-weighted isotopic signatures by source category. Given values are averages over 1998-2018. Numbers in brackets are minimum and maximum over this period of time [min/max].

Categories	Prior CH_4 emissions ($TgCH_4.yr^{-1}$)	Prior isotopic signatures (‰ - VPDB)	Posterior CH_4 emissions ($TgCH_4.yr^{-1}$)	Posterior isotopic signatures (‰ - VPDB)
BB	27 [24 / 35]	-22.3 [-22.5 / -22.2]	28 [23 / 44]	-21.5 [-22.2 / -21.3]
AGW	213 [195 / 232]	-59.1 [-59.2 / -59.0]	221 [197 / 241]	-58.3 [-59.4 / -57.0]
FFG	117 [99 / 133]	-44.9 [-45.6 / -44.3]	124 [101 / 142]	-43.5 [-44.8 / -42.1]
NAT	23 [23 / 23]	-50.7 [-50.7 / -50.7]	23 [23 / 23]	-50.8 [-50.8 / -50.8]
WET	180 [180 - 181]	-60.8 [-60.8 / -60.8]	192 [184 / 202]	-56.6 [-56.6 / -56.5]
Total	560 [520 - 597]	-54.4 [-54.9 / -53.8]	588 [530 / 639]	-52.6 [-53.3 / -52.0]

Table S2. Global flux-weighted values and references for $\delta^{13}C(CH4)_{source}$ source signatures associated to the different emission categories and subcategories. * Values are prescribed at regional or pixel scale (see Fig. S2).

E19 : (Etiope et al., 2019) ; CH19 : Chang et al. (2019) ; GA18 : Ganesan et al. (2018) ; TH18 : Thompson et al. (2018) ; SH17 : Sherwood et al. (2017) ; SH16 : Schwietzke et al. (2016) ; WA16 : Warwick et al. (2016) ; ZA16 : Zazzeri et al. (2016) ; TO12 : Townsend-Small et al. (2012) ; KL10 : Klevenhusen et al. (2010) ; BO06 : Bousquet et al. (2006) ; BR01 : Bréas et al. (2001) ; SA01 : Sansone et al. (2001) ; CH00 : Chanton et al. (2000) ; HO00 : Holmes et al. (2000) ; CH99 : Chanton et al. (1999) ; BE98 : Bergamaschi et al. (1998) ; LE93 : Levin et al. (1993);

Categories	Global signatures (‰)	Subcategories	Global signature (‰)	References
AGW	-59.1 *	Rice cultivation	-63.0	SH17; BO06; BR01
		Enteric fermentation	-64.7 *	CH19
		Agriculture waste	-52.0	KL10 ; LE93
		Landfills	-52.0	TO12 ; CH99 ; BE98 ; LE93
		Waste water	-48.0	TO12 ; CH99 ; BE98 ; LE93
FFG	-44.9 *	Oil and gas	-44.9 *	SH07
		Coal	-42.3 *	SH07 ; ZA16
		Geological sources	-49	E19
BB	-22.3 *	Biomass burning	-24.9 *	BO06 ; CH00
		Biofuel burning	-20	CH00
WET	-60.8 *	Wetlands	-60.8 *	GA18
NAT	-50.7 *	Oceanic sources	-42	BR01; HO00 ; SA01
		Termites	-63	TH18; SH16 ; SH17; WA16

Table S3. Sink intensities and associated fractionation coefficients (KIE) for the period 1998-2018. Numbers in brackets are minimum and maximum over this period of time [min/max].

Species	Sink ($TgCH_4.yr^{-1}$)	KIE (k_{12} / k_{13})	Reference
OH	524 [498 - 550]	1.0039	Saueressig et al. (2001)
$O(^1D)$	8 [7- 8]	1.013	Saueressig et al. (2001)
Cl	9 [8 - 9]	1.043·exp(6.455/T)	Saueressig et al. (1995)
Soils	39 [38 - 40]	1.020	Snover and Quay (2000) Reeburgh et al. (1997) Tyler et al. (1994) King et al. (1989)
Total	579 [552 - 605]	1.0053	

Table S4. Providers, locations and number of vertical profiles of CH_4 retrieved using AirCore technique between 2012 and 2018. The longitude and latitude given here are means over the AirCore descent profile.

Provider	Location	Number of profiles	Longitude	Latitude
NOAA-ESRL Aircraft Program	Edwards AFB/Dryden, USA	6	117.51° W	34.58° N
	Boulder, CO, USA	33	104.34° W	39.53° N
	Lamont, OK, USA	30	97.45° W	36.65° N
	Park Falls, WI, USA	4	90.27° W	46.03° N
	Sodankylä, Finland	6	25.97° E	67.60° N
	Lauder, NZ	1	170.01° E	45.19° S
French AirCore Program	Alice Springs, Australia	3	132.58° E	23.66° S
	Aire-sur-l'Adour, France	9	1.02° E	43.25° N
	Trainou, France	17	1.86° E	47.30° N
	Timmins, Ontario, Canada	4	83.28° W	48.49° N
	Esrange, Northern Sweden	2	22.86° E	67.87° N

Table S5. List of CH_4 surface in-situ observation sites that provided measurements assimilated in the inversion between 1998 and 2018. AOC, PAO, POC et WPC are mobile stations. Their characteristics are compiled into a single line, providing latitude and longitude ranges of the measurements. Stations that retrieved samples consisting mainly of well-mixed Marine Boundary Layer (MBL) air are indicated in bold red.

Site code	Station name	Country/Territory	Network	Latitude	Longitude	Elevation (m a.s.l.)	Date range (MM/YYYY)
ABP	Arembepe	Brazil	NOAA	12.76° S	38.16° W	6	10/2006 - 01/2010
ALT	Alert	Canada	NOAA	82.45° N	62.51° W	195	01/1998 - 12/2018
AMT	Argyle	United States	NOAA	45.03° N	68.68° W	157	09/2003 - 12/2008
AMY	Anmyeon-do	Republic of Korea	NOAA	36.54° N	126.33° E	125	12/2013 - 12/2018
AOC	Atlantic Ocean Cruise	N/A	NOAA	30.30° S 35.00° N	-75.11° W 13.57° E	22	05/2004 - 02/2005
ASC	Ascension Island	United Kingdom	NOAA	7.97° S	14.40° W	90	01/1998 - 12/2018
ASK	Assekrem	Algeria	NOAA	23.26° N	5.63° E	2715	01/1998 - 12/2018
AZR	Terceira Island	Portugal	NOAA	38.77° N	27.38° W	24	01/1998 - 12/2018
BAL	Baltic Sea	Poland	NOAA	55.43° N	16.95° E	28	01/1998 - 06/2011
BHD	Baring Head Station	New Zealand	NOAA	41.41° S	174.87° E	90	10/1999 - 12/2018
BKT	Bukit Kototabang	Indonesia	NOAA	0.20° S	100.32° E	875	01/2004 - 12/2018
BME	St. Davids Head	United Kingdom	NOAA	32.37° N	64.65° W	17	01/1998 - 01/2010
BMW	Tudor Hill	United Kingdom	NOAA	32.26° N	64.88° W	60	01/1998 - 12/2018
BRW	Barrow Atmospheric Baseline Observatory	United States	NOAA	71.32° N	156.60° W	13	01/1998 - 12/2018
BSC	Black Sea	Romania	NOAA	44.18° N	28.66° E	5	01/1998 - 12/2011
CBA	Cold Bay	United States	NOAA	55.20° N	162.72° W	25	01/1998 - 12/2018
CGO	Cape Grim	Australia	NOAA	40.68° S	144.68° E	164	01/1998 - 12/2018
CHR	Christmas Island	Republic of Kiribati	NOAA	1.70° N	157.15° W	5	11/1998 - 12/2018
CIB	Centro de Investigacion de la Baja Atmosfera (CIBA)	Spain	NOAA	41.81° N	4.93° W	850	05/2009 - 12/2018
CMO	Cape Meares	United States	NOAA	45.48° N	123.97° W	35	03/1998 - 03/1998
CPT	Cape Point	South Africa	NOAA	34.35° S	18.49° E	260	02/2010 - 12/2018
CRZ	Crozet Island	France	NOAA	46.43° S	51.85° E	202	01/1998 - 11/2018
DRP	Drake Passage	nan	NOAA	57.65° S	64.18° W	10	04/2003 - 12/2018
DSI	Dongsha Island	Taiwan	NOAA	20.70° N	116.73° E	8	03/2010 - 12/2018
EIC	Easter Island	Chile	NOAA	27.15° S	109.45° W	55	01/1998 - 12/2018
GMI	Mariana Islands	Guam	NOAA	13.39° N	144.66° E	6	01/1998 - 12/2018
GOZ	Dwejra Point	Malta	NOAA	36.05° N	14.89° E	6	01/1998 - 02/1999
HBA	Halley Station	United Kingdom	NOAA	75.61° S	26.21° W	35	01/1998 - 02/2018
HPB	Hohenpeissenberg	Germany	NOAA	47.80° N	11.02° E	990	04/2006 - 12/2018
HSU	Humboldt State University	United States	NOAA	41.05° N	124.73° W	7	05/2008 - 05/2017

Table S5. Following Table S5

Site code	Station name	Country/Territory	Network	Latitude	Longitude	Elevation (m a.s.l.)	Date range (MM/YYYY)
HUN	Hegyhatsal	Hungary	NOAA	46.95° N	16.65° E	344	01/1998 - 12/2018
ICE	Storhofdi	Iceland	NOAA	63.40° N	20.29° W	127	01/1998 - 12/2018
ITN	Grifton	United States	NOAA	35.37° N	77.39° W	505	01/1998 - 06/1999
IZO	Izana	Spain	NOAA	28.30° N	16.48° W	2377	01/1998 - 12/2018
KCO	Kaashidhoo	Republic of Maldives	NOAA	4.97° N	73.47° E	6	03/1998 - 07/1999
KEY	Key Biscayne	United States	NOAA	25.67° N	80.20° W	6	01/1998 - 12/2018
KUM	Cape Kumukahi	United States	NOAA	19.52° N	154.82° W	8	01/1998 - 12/2018
KZD	Sary Taukum	Kazakhstan	NOAA	44.45° N	75.57° E	412	01/1998 - 08/2009
KZM	Plateau Assy	Kazakhstan	NOAA	43.25° N	77.88° E	2524	01/1998 - 08/2009
LEF	Park Falls	United States	NOAA	45.93° N	90.27° W	868	01/1998 - 12/2018
LLB	Lac La Biche	Canada	NOAA	54.95° N	112.45° W	546	01/2008 - 02/2013
LLN	Lulin	Taiwan	NOAA	23.46° N	120.86° E	2867	08/2006 - 12/2018
LMP	Lampedusa	Italy	NOAA	35.51° N	12.61° E	50	10/2006 - 12/2018
MEX	High Altitude Global Climate Observation Center	Mexico	NOAA	18.98° N	97.31° W	4469	01/2009 - 12/2018
MHD	Mace Head	Ireland	NOAA	53.33° N	9.90° W	26	01/1998 - 12/2018
MID	Sand Island	United States	NOAA	28.22° N	177.37° W	8	01/1998 - 12/2018
MKN	Mt. Kenya	Kenya	NOAA	0.06° S	37.30° E	3649	12/2003 - 06/2011
MLO	Mauna Loa	United States	NOAA	19.53° N	155.58° W	3437	01/1998 - 12/2018
NAT	Farol De Mae Luiza Lighthouse	Brazil	NOAA	5.51° S	35.26° W	20	09/2010 - 12/2018
NMB	Gobabeb	Namibia	NOAA	23.58° S	15.03° E	461	07/1998 - 12/2018
NWR	Niwot Ridge	United States	NOAA	40.05° N	105.58° W	3526	01/1998 - 12/2018
OXK	Ochsenkopf	Germany	NOAA	50.03° N	11.81° E	1185	03/2003 - 12/2018
PAL	Pallas-Sammaltunturi	Finland	NOAA	67.97° N	24.12° E	570	12/2001 - 12/2018
PAO	Pacific-Atlantic Ocean	N/A	NOAA	30.20° S 67.86° N	164.58° W 9.93° W	10	03/2006 - 10/2006
POC	Pacific Ocean	N/A	NOAA	36.67° S 35.07° N	180.00° W 179.83° E	20	04/1998 - 07/2017
PSA	Palmer Station	United States	NOAA	64.92° S	64.00° W	15	01/1998 - 12/2018
PTA	Point Arena	United States	NOAA	38.95° N	123.73° W	22	01/1999 - 05/2011
RPB	Ragged Point	Barbados	NOAA	13.16° N	59.43° W	20	01/1998 - 12/2018
SDZ	Shangdianzi	Peoples Republic of China	NOAA	40.65° N	117.12° E	298	09/2009 - 09/2015
SEY	Mahe Island	Seychelles	NOAA	4.68° S	55.53° E	7	01/1998 - 12/2018

Table S5. Following Table S5

Site code	Station name	Country/Territory	Network	Latitude	Longitude	Elevation (m a.s.l.)	Date range (MM/YYYY)
SGP	Southern Great Plains	United States	NOAA	36.62° N	97.48° W	374	04/2002 - 12/2018
SHM	Shemya Island	United States	NOAA	52.72° N	174.10° E	28	01/1998 - 10/2018
SMO	Tutuila	American Samoa	NOAA	14.25° S	170.57° W	47	01/1998 - 12/2018
SPO	South Pole	United States	NOAA	89.98° S	24.80° W	2821	01/1998 - 12/2018
STM	Ocean Station M	Norway	NOAA	66.00° N	2.00° E	7	01/1998 - 11/2009
SUM	Summit	Greenland	NOAA	72.60° N	38.42° W	3214	01/1998 - 12/2018
SYO	Syowa Station	Japan	NOAA	69.00° S	39.58° E	16	01/1998 - 12/2018
TAC	Tacolneston	United Kingdom	NOAA	52.52° N	1.14° E	236	06/2014 - 01/2016
TAP	Tae-ahn Peninsula	Republic of Korea	NOAA	36.73° N	126.13° E	21	01/1998 - 12/2018
THD	Trinidad Head	United States	NOAA	41.05° N	124.15° W	112	04/2002 - 06/2017
TIK	Hydrometeorological Observatory of Tiksi	Russia	NOAA	71.60° N	128.89° E	29	08/2011 - 09/2018
USH	Ushuaia	Argentina	NOAA	54.85° S	68.31° W	32	01/1998 - 12/2018
UTA	Wendover	United States	NOAA	39.90° N	113.72° W	1332	01/1998 - 12/2018
UUM	Ulaan Uul	Mongolia	NOAA	44.45° N	111.10° E	1012	01/1998 - 12/2018
WIS	Weizmann Institute of Science at the Arava Institute	Israel	NOAA	30.86° N	34.78° E	482	01/1998 - 12/2018
WKT	Moody	United States	NOAA	31.32° N	97.33° W	708	02/2001 - 10/2010
WLG	Mt. Waliguan	Peoples Republic of China	NOAA	36.27° N	100.92° E	3815	01/1998 - 12/2018
WPC	Western Pacific Cruise	N/A	NOAA	30.67° S 32.46° N	135.55° E 170.47° E	8	05/2004 - 06/2013
ZEP	Ny-Alesund	Norway and Sweden	NOAA	78.91° N	11.89° E	479	01/1998 - 12/2018

Table S6. List of $\delta^{13}C(CH_4)$ surface in-situ observation sites that provided measurements assimilated in the inversion between 1998 and 2018. WPC is a mobile station. Its characteristics are compiled into a single line, providing latitude and longitude ranges of the measurements. Stations that retrieved samples consisting mainly of well-mixed MBL air are indicated in bold red.

Site code	Station name	Country/Territory	Network	Latitude	Longitude	Elevation (m a.s.l.)	Date range (MM/YYYY)
ALT	Alert	Canada	NOAA	82.45° N	62.51° W	195	08/2000 - 12/2017
AMY	Anmyeon-do	Republic of Korea	NOAA	36.54° N	126.33° E	125	12/2013 - 12/2017
ASC	Ascension Island	United Kingdom	NOAA	7.97° S	14.40° W	90	10/2000 - 12/2017
AZR	Terceira Island	Portugal	NOAA	38.75° N	27.08° W	24	08/2000 - 12/2017
BAL	Baltic Sea	Poland	NOAA	55.35° N	17.22° E	28	04/2008 - 06/2011
BHD	Baring Head Station	New Zealand	NOAA	41.41° S	174.87° E	90	03/2009 - 11/2017
BRW	Barrow Atmospheric Baseline Observatory	United States	NOAA	71.32° N	156.60° W	16	01/1998 - 12/2017
CBA	Cold Bay	United States	NOAA	55.20° N	162.72° W	25	08/2000 - 12/2017
CGO	Cape Grim	Australia	NOAA	40.68° S	144.68° E	164	01/1998 - 12/2017
KUM	Cape Kumukahi	United States	NOAA	19.52° N	154.82° W	3	01/1999 - 12/2017
LLB	Lac La Biche	Canada	NOAA	54.95° N	112.45° W	546	01/2008 - 02/2013
MEX	High Altitude Global Climate Observation Center	Mexico	NOAA	18.98° N	97.31° W	4469	01/2009 - 12/2017
MHD	Mace Head	Ireland	NOAA	53.33° N	9.90° W	26	01/1999 - 12/2017
MLO	Mauna Loa	United States	NOAA	19.53° N	155.58° W	3402	01/1998 - 12/2017
NWR	Niwot Ridge	United States	NOAA	40.05° N	105.58° W	3526	01/1998 - 12/2017
SMO	Tutuila	American Samoa	NOAA	14.25° S	170.57° W	47	01/1998 - 12/2017
SPO	South Pole	United States	NOAA	89.98° S	24.80° W	2815	01/1998 - 12/2017
SUM	Summit	Greenland	NOAA	72.60° N	38.42° W	3214	04/2010 - 12/2017
TAP	Tae-ahn Peninsula	Republic of Korea	NOAA	36.73° N	126.13° E	21	09/2000 - 12/2017
WLG	Mt. Waliguan	Peoples Republic of China	NOAA	36.27° N	100.92° E	3815	07/2001 - 12/2017
WPC	Western Pacific Cruise	N/A	NOAA	30.35° S	167.73° E	10	11/2005 - 06/2013
ZEP	Ny-Alesund	Norway and Sweden	NOAA	78.91° N	11.89° E	479	10/2001 - 12/2017

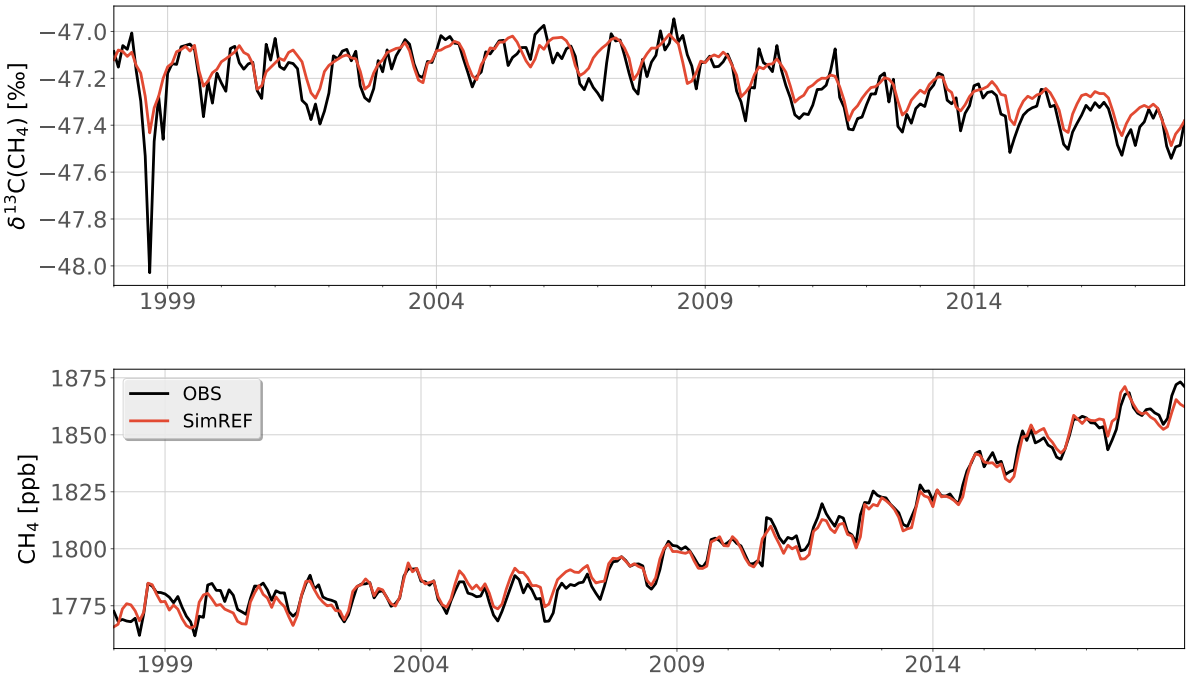

Figure S1. Time-series of observed and simulated CH_4 and $\delta^{13}C(CH_4)$ monthly values averaged over the globe using latitudinal band average. Simulated values are outputs from SimREF.

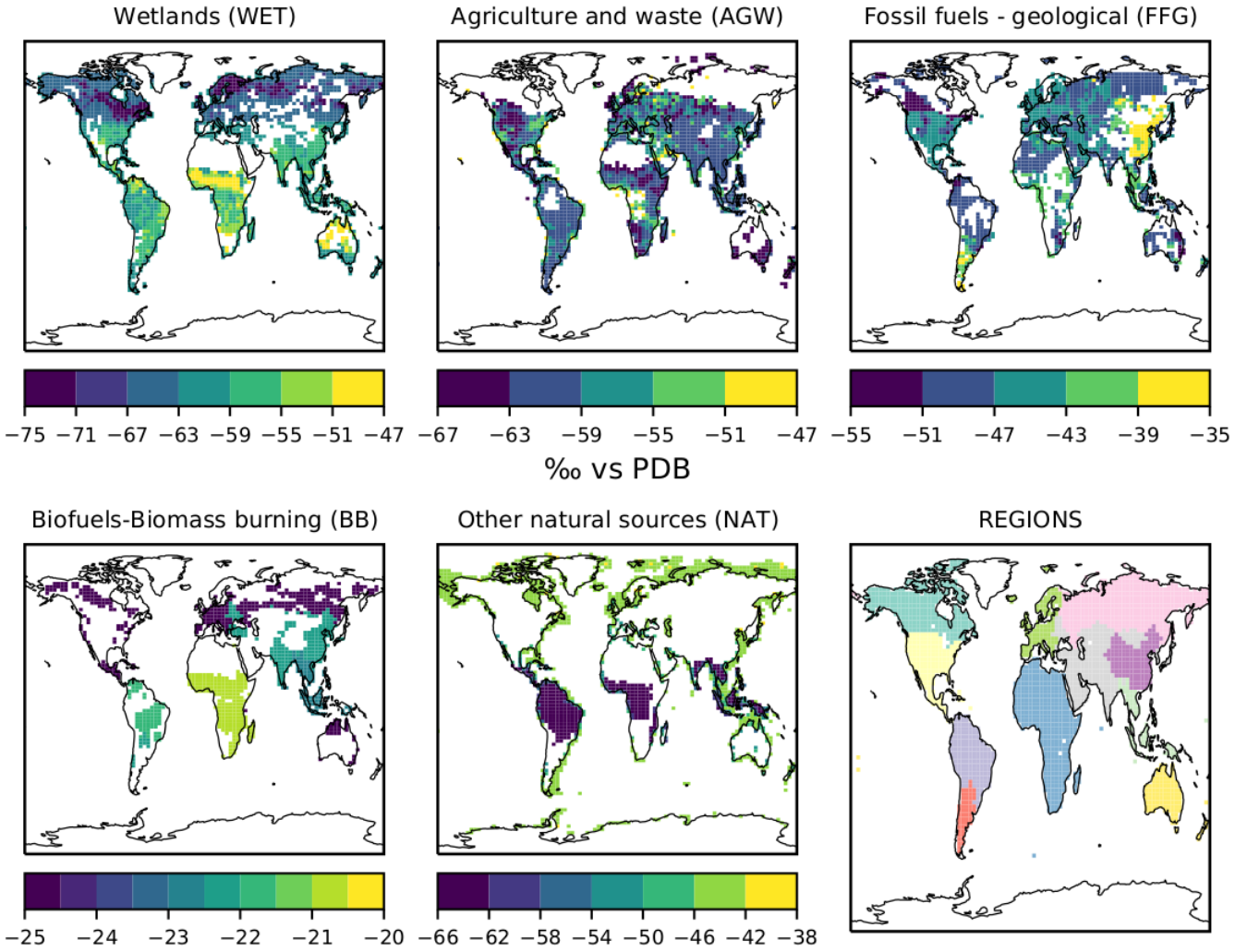

Figure S2. Prior estimates of $\delta^{13}C(CH4)_{source}$ isotopic signatures for each of the five emission categories averaged over the 1998-2018 period. The regions over which the values are optimized are shown in the lower-right panel. WET source signatures are dependent on the latitude, with more depleted values in boreal regions than in tropical regions. BB source signatures are dependent on the vegetation (C3/C4). Burning C4 vegetation tropical regions releases CH4 that is more ^{13}C-enriched than CH4 released when burning C3 vegetation. AGW source signatures is dependent on the country/region and the C3 versus C4 livestock diet. FFG source signatures mainly depend both on the location and the contributions from coal, oil&gas and geological sources to the total FFG emissions of a specific country/region. For example, China ^{13}C-enriched large coal emissions highly contributes to the FFG source signature in this region which is notably ^{13}C-enriched compared to other regions.

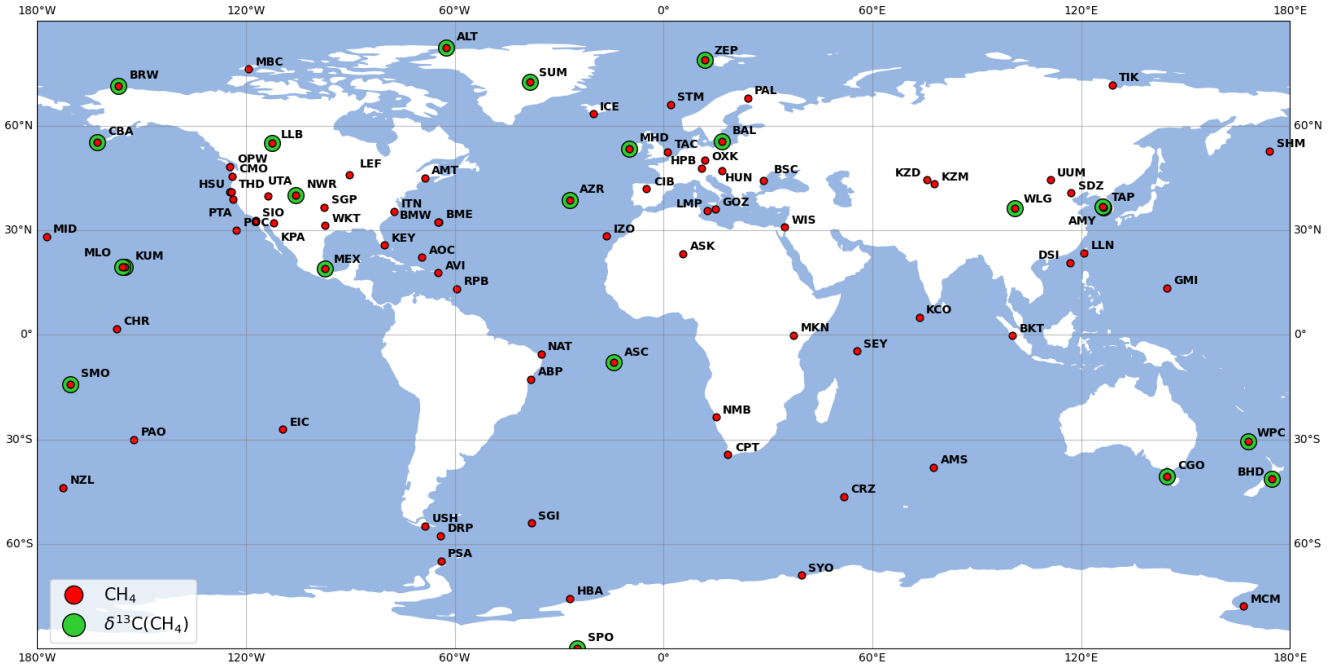

Figure S3. Locations of CH_4 and $\delta^{13}C(CH_4)$ surface stations. Affiliated networks are not displayed. More information about the stations can be found in Table S5 and Table S6.

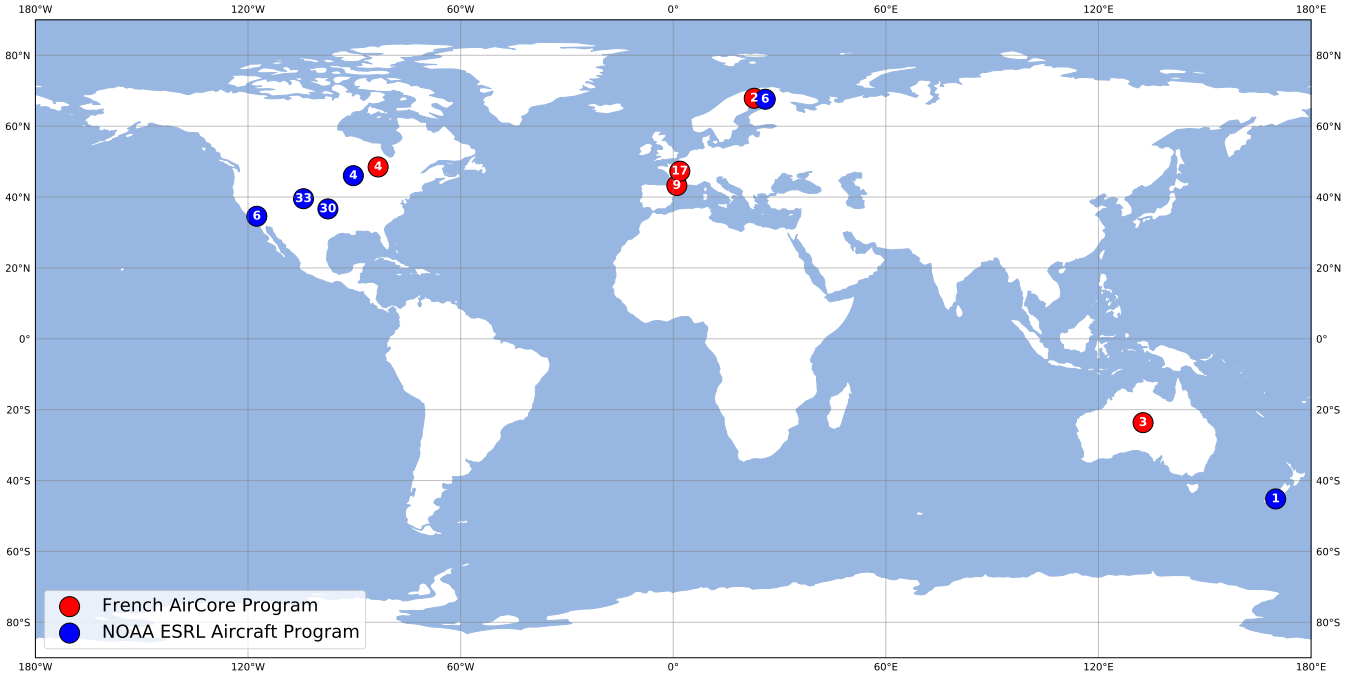

Figure S4. Locations and numbers of CH_4 vertical profiles retrieved using the AirCore technique. A comprehensive list of the locations and the associated providers can be found in Table S4.

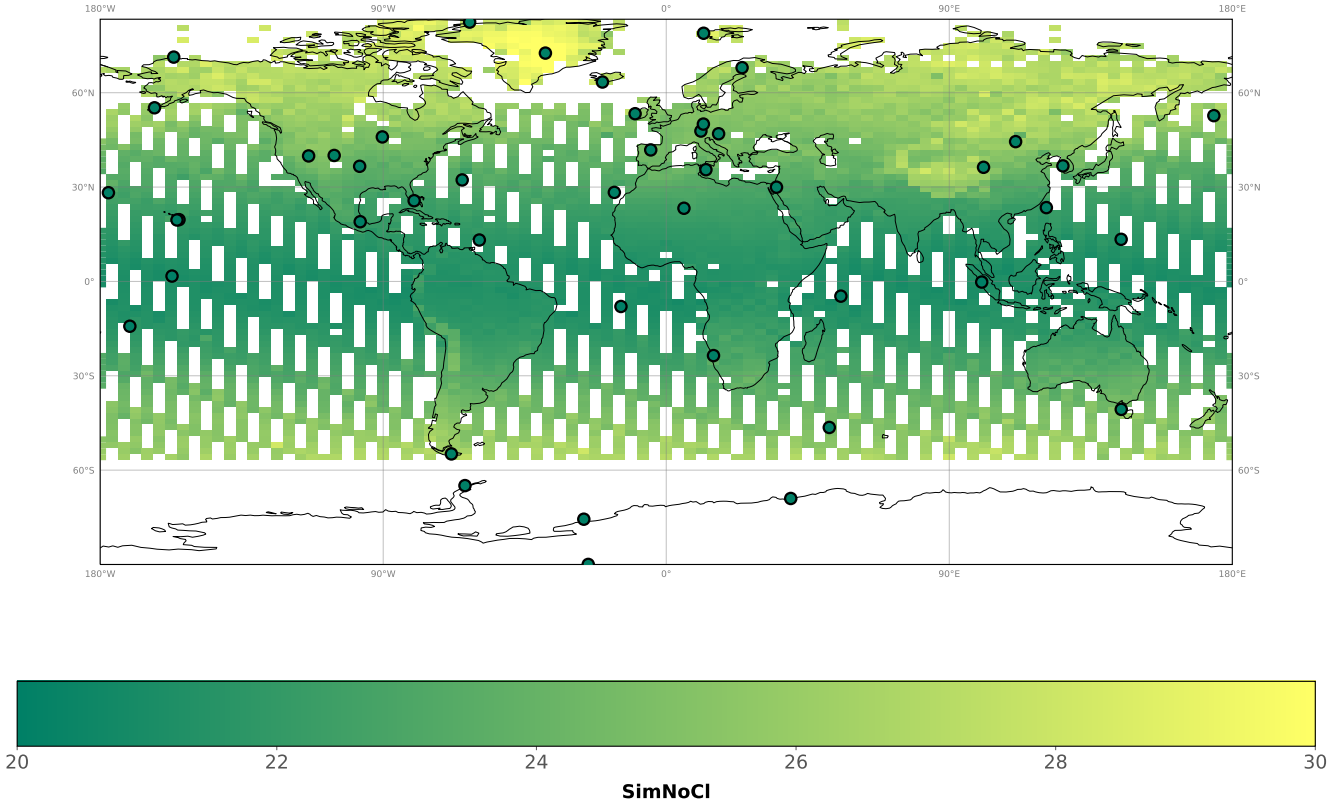

Figure S5. XCH_4 annual bias in 2018 between SimNoCl and SimREF. Colored dots show the bias at NOAA GML surface stations.

References

Bergamaschi, P., Lubina, C., Königstedt, R., Fischer, H., Veltkamp, A. C., and Zwaagstra, O.: Stable isotopic signatures (δ^{13}C, δD) of methane from European landfill sites, Journal of Geophysical Research: Atmospheres, 103, 8251–8265, https://doi.org/10.1029/98JD00105, 1998.

Bousquet, P., Ciais, P., Miller, J. B., Dlugokencky, E. J., Hauglustaine, D. A., Prigent, C., Van der Werf, G. R., Peylin, P., Brunke, E.-G., Carouge, C., Langenfelds, R. L., Lathière, J., Papa, F., Ramonet, M., Schmidt, M., Steele, L. P., Tyler, S. C., and White, J.: Contribution of anthropogenic and natural sources to atmospheric methane variability, Nature, 443, 439–443, https://doi.org/10.1038/nature05132, 2006.

Bréas, O., Guillou, C., Reniero, F., and Wada, E.: The Global Methane Cycle: Isotopes and Mixing Ratios, Sources and Sinks, Isotopes in Environmental and Health Studies, 37, 257–379, https://doi.org/10.1080/10256010108033302, 2001.

Chang, J., Peng, S., Ciais, P., Saunois, M., Dangal, S. R. S., Herrero, M., Havlík, P., Tian, H., and Bousquet, P.: Revisiting enteric methane emissions from domestic ruminants and their $\delta^{13}CCH_4$ source signature, Nature Communications, 10, 3420, https://doi.org/10.1038/s41467-019-11066-3, 2019.

Chanton, J. P., Rutkowski, C. M., and Mosher, B.: Quantifying Methane Oxidation from Landfills Using Stable Isotope Analysis of Downwind Plumes, Environmental Science & Technology, 33, 3755–3760, https://doi.org/10.1021/es9904033, 1999.

Chanton, J. P., Rutkowski, C. M., Schwartz, C. C., Ward, D. E., and Boring, L.: Factors influencing the stable carbon isotopic signature of methane from combustion and biomass burning, Journal of Geophysical Research: Atmospheres, 105, 1867–1877, https://doi.org/10.1029/1999JD900909, 2000.

Etiope, G.: Natural Gas Seepage: The Earth's Hydrocarbon Degassing, Springer International Publishing, https://www.springer.com/gp/book/9783319146003, 2015.

Etiope, G., Ciotoli, G., Schwietzke, S., and Schoell, M.: Gridded maps of geological methane emissions and their isotopic signature, https://doi.org/10.5194/essd-11-1-2019, 2019.

Folberth, G. A., Hauglustaine, D. A., Lathière, J., and Brocheton, F.: Interactive chemistry in the Laboratoire de Météorologie Dynamique general circulation model: model description and impact analysis of biogenic hydrocarbons on tropospheric chemistry, Atmospheric Chemistry and Physics, 6, 2273–2319, https://doi.org/10.5194/acp-6-2273-2006, 2006.

Ganesan, A. L., Stell, A. C., Gedney, N., Comyn-Platt, E., Hayman, G., Rigby, M., Poulter, B., and Hornibrook, E. R. C.: Spatially Resolved Isotopic Source Signatures of Wetland Methane Emissions, Geophysical Research Letters, 45, 3737–3745, https://doi.org/10.1002/2018GL077536, 2018.

Gilbert, J. C. and Lemaréchal, C.: Some numerical experiments with variable-storage quasi-Newton algorithms, Mathematical Programming, 45, 407–435, https://doi.org/10.1007/BF01589113, 1989.

Hauglustaine, D. A., Hourdin, F., Jourdain, L., Filiberti, M.-A., Walters, S., Lamarque, J.-F., and Holland, E. A.: Interactive chemistry in the Laboratoire de Météorologie Dynamique general circulation model: Description and background tropospheric chemistry evaluation, Journal of Geophysical Research: Atmospheres, 109, https://doi.org/10.1029/2003JD003957, 2004.

Hauglustaine, D. A., Cozic, A., Caubel, A., Lathière, J., Sépulchre, P., Cohen, Y., Balkanski, Y., Lurton, T., Boucher, O., and Tsigaridis, K.: Coupled Climate-Chemistry-Aerosol simulations under the AerChemMIP scenarios with the IPSL-CM5A2-INCA climate model, in preparation, 2021.

Holmes, M. E., Sansone, F. J., Rust, T. M., and Popp, B. N.: Methane production, consumption, and air-sea exchange in the open ocean: An Evaluation based on carbon isotopic ratios, Global Biogeochemical Cycles, 14, 1–10, https://doi.org/10.1029/1999GB001209, 2000.

King, S. L., Quay, P. D., and Lansdown, J. M.: The $^{13}C/^{12}C$ kinetic isotope effect for soil oxidation of methane at ambient atmospheric concentrations, Journal of Geophysical Research: Atmospheres, 94, 18 273–18 277, https://doi.org/10.1029/JD094iD15p18273, 1989.

Kirschke, S., Bousquet, P., Ciais, P., Saunois, M., Canadell, J. G., Dlugokencky, E. J., Bergamaschi, P., Bergmann, D., Blake, D. R., Bruhwiler, L., Cameron-Smith, P., Castaldi, S., Chevallier, F., Feng, L., Fraser, A., Heimann, M., Hodson, E. L., Houweling, S., Josse, B., Fraser, P. J., Krummel, P. B., Lamarque, J.-F., Langenfelds, R. L., Le Quéré, C., Naik, V., O'Doherty, S., Palmer, P. I., Pison, I., Plummer, D., Poulter, B., Prinn, R. G., Rigby, M., Ringeval, B., Santini, M., Schmidt, M., Shindell, D. T., Simpson, I. J., Spahni, R., Steele, L. P., Strode, S. A., Sudo, K., Szopa, S., van der Werf, G. R., Voulgarakis, A., van Weele, M., Weiss, R. F., Williams, J. E., and Zeng, G.: Three decades of global methane sources and sinks, Nature Geoscience, 6, 813–823, https://doi.org/10.1038/ngeo1955, 2013.

Klevenhusen, F., Bernasconi, S. M., Kreuzer, M., and Soliva, C. R.: Experimental validation of the Intergovernmental Panel on Climate Change default values for ruminant-derived methane and its carbon-isotope signature, Animal Production Science, 50, 159, https://doi.org/10.1071/AN09112, 2010.

Kuze, A., Suto, H., Nakajima, M., and Hamazaki, T.: Thermal and near infrared sensor for carbon observation Fourier-transform spectrometer on the Greenhouse Gases Observing Satellite for greenhouse gases monitoring, Applied Optics, 48, 6716–6733, https://doi.org/10.1364/AO.48.006716, 2009.

Lambert, G. and Schmidt, S.: Reevaluation of the oceanic flux of methane: Uncertainties and long term variations, Chemosphere, 26, 579–589, https://doi.org/10.1016/0045-6535(93)90443-9, 1993.

Levin, I., Bergamaschi, P., Dörr, H., and Trapp, D.: Stable isotopic signature of methane from major sources in Germany, Chemosphere, 26, 161–177, https://doi.org/10.1016/0045-6535(93)90419-6, 1993.

Meinshausen, M., Vogel, E., Nauels, A., Lorbacher, K., Meinshausen, N., Etheridge, D. M., Fraser, P. J., Montzka, S. A., Rayner, P. J., Trudinger, C. M., Krummel, P. B., Beyerle, U., Canadell, J. G., Daniel, J. S., Enting, I. G., Law, R. M., Lunder, C. R., O'Doherty, S., Prinn, R. G., Reimann, S., Rubino, M., Velders, G. J. M., Vollmer, M. K., Wang, R. H. J., and Weiss, R.: Historical greenhouse gas concentrations for climate modelling (CMIP6), Geoscientific Model Development, 10, 2057–2116, https://doi.org/https://doi.org/10.5194/gmd-10-2057-2017, 2017.

Ostler, A., Sussmann, R., Patra, P. K., Houweling, S., Bruine, M. D., Stiller, G. P., Haenel, F. J., Plieninger, J., Bousquet, P., Yin, Y., Saunois, M., Walker, K. A., Deutscher, N. M., Griffith, D. W. T., Blumenstock, T., Hase, F., Warneke, T., Wang, Z., Kivi, R., and Robinson, J.: Evaluation of column-averaged methane in models and TCCON with a focus on the stratosphere, Atmospheric Measurement Techniques, 9, 4843–4859, https://doi.org/https://doi.org/10.5194/amt-9-4843-2016, 2016.

Parker, R. J., Webb, A., Boesch, H., Somkuti, P., Barrio Guillo, R., Di Noia, A., Kalaitzi, N., Anand, J. S., Bergamaschi, P., Chevallier, F., Palmer, P. I., Feng, L., Deutscher, N. M., Feist, D. G., Griffith, D. W. T., Hase, F., Kivi, R., Morino, I., Notholt, J., Oh, Y.-S., Ohyama, H., Petri, C., Pollard, D. F., Roehl, C., Sha, M. K., Shiomi, K., Strong, K., Sussmann, R., Té, Y., Velazco, V. A., Warneke, T., Wennberg, P. O., and Wunch, D.: A decade of GOSAT Proxy satellite CH_4 observations, Earth System Science Data, 12, 3383–3412, https://doi.org/https://doi.org/10.5194/essd-12-3383-2020, 2020.

Poulter, B., Bousquet, P., Canadell, J. G., Ciais, P., Peregon, A., Saunois, M., Arora, V. K., Beerling, D. J., Brovkin, V., Jones, C. D., Joos, F., Gedney, N., Ito, A., Kleinen, T., Koven, C. D., McDonald, K., Melton, J. R., Peng, C., Peng, S., Prigent, C., Schroeder, R., Riley, W. J., Saito, M., Spahni, R., Tian, H., Taylor, L., Viovy, N., Wilton, D., Wiltshire, A., Xu, X., Zhang, B., Zhang, Z., and Zhu, Q.: Global wetland contribution to 2000–2012 atmospheric methane growth rate dynamics, Environmental Research Letters, 12, 094 013, https://doi.org/10.1088/1748-9326/aa8391, 2017.

Reeburgh, W. S., Hirsch, A. I., Sansone, F. J., Popp, B. N., and Rust, T. M.: Carbon kinetic isotope effect accompanying microbial oxidation of methane in boreal forest soils, Geochimica et Cosmochimica Acta, 61, 4761–4767, https://doi.org/10.1016/S0016-7037(97)00277-9, 1997.

Ridgwell, A. J., Marshall, S. J., and Gregson, K.: Consumption of atmospheric methane by soils: A process-based model, Global Biogeochemical Cycles, 13, 59–70, https://doi.org/10.1029/1998GB900004, 1999.

Sansone, F. J., Popp, B. N., Gasc, A., Graham, A. W., and Rust, T. M.: Highly elevated methane in the eastern tropical North Pacific and associated isotopically enriched fluxes to the atmosphere, Geophysical Research Letters, 28, 4567–4570, https://doi.org/10.1029/2001GL013460, 2001.

Saueressig, G., Bergamaschi, P., Crowley, J. N., Fischer, H., and Harris, G. W.: Carbon kinetic isotope effect in the reaction of CH_4 with Cl atoms, Geophysical Research Letters, 22, 1225–1228, https://doi.org/10.1029/95GL00881, 1995.

Saueressig, G., Crowley, J. N., Bergamaschi, P., Brühl, C., Brenninkmeijer, C. A. M., and Fischer, H.: Carbon 13 and D kinetic isotope effects in the reactions of CH_4 with O(1 D) and OH: New laboratory measurements and their implications for the isotopic composition of stratospheric methane, Journal of Geophysical Research: Atmospheres, 106, 23 127–23 138, https://doi.org/10.1029/2000JD000120, 2001.

Saunois, M., Stavert, A. R., Poulter, B., Bousquet, P., Canadell, J. G., Jackson, R. B., Raymond, P. A., Dlugokencky, E. J., Houweling, S., Patra, P. K., Ciais, P., Arora, V. K., Bastviken, D., Bergamaschi, P., Blake, D. R., Brailsford, G., Bruhwiler, L., Carlson, K. M., Carrol, M., Castaldi, S., Chandra, N., Crevoisier, C., Crill, P. M., Covey, K., Curry, C. L., Etiope, G., Frankenberg, C., Gedney, N., Hegglin, M. I., Höglund-Isaksson, L., Hugelius, G., Ishizawa, M., Ito, A., Janssens-Maenhout, G., Jensen, K. M., Joos, F., Kleinen, T., Krummel, P. B., Langenfelds, R. L., Laruelle, G. G., Liu, L., Machida, T., Maksyutov, S., McDonald, K. C., McNorton, J., Miller, P. A., Melton, J. R., Morino, I., Müller, J., Murguia-Flores, F., Naik, V., Niwa, Y., Noce, S., O'Doherty, S., Parker, R. J., Peng, C., Peng, S., Peters, G. P., Prigent, C., Prinn, R., Ramonet, M., Regnier, P., Riley, W. J., Rosentreter, J. A., Segers, A., Simpson, I. J., Shi, H., Smith, S. J., Steele, L. P., Thornton, B. F., Tian, H., Tohjima, Y., Tubiello, F. N., Tsuruta, A., Viovy, N., Voulgarakis, A., Weber, T. S., van Weele, M., van der Werf, G. R., Weiss, R. F., Worthy, D., Wunch, D., Yin, Y., Yoshida, Y., Zhang, W., Zhang, Z., Zhao, Y., Zheng, B., Zhu, Q., Zhu, Q., and Zhuang, Q.: The Global Methane Budget 2000–2017, Earth System Science Data, 12, 1561–1623, https://doi.org/https://doi.org/10.5194/essd-12-1561-2020, 2020.

Schwietzke, S., Sherwood, O. A., Bruhwiler, L. M. P., Miller, J. B., Etiope, G., Dlugokencky, E. J., Michel, S. E., Arling, V. A., Vaughn, B. H., White, J. W. C., and Tans, P. P.: Upward revision of global fossil fuel methane emissions based on isotope database, Nature, 538, 88–91, https://doi.org/10.1038/nature19797, 2016.

Sherwood, O. A., Schwietzke, S., Arling, V. A., and Etiope, G.: Global Inventory of Gas Geochemistry Data from Fossil Fuel, Microbial and Burning Sources, version 2017, Earth System Science Data, 9, 639–656, https://doi.org/10.5194/essd-9-639-2017, 2017.

Snover, A. K. and Quay, P. D.: Hydrogen and carbon kinetic isotope effects during soil uptake of atmospheric methane, Global Biogeochemical Cycles, 14, 25–39, https://doi.org/10.1029/1999GB900089, 2000.

Terrenoire, E., Hauglustaine, D., Gasser, T., and Penanhoat, O.: The impact of carbon dioxide aviation emissions on future climate change, in: 1st Edition of the Aerospace Europe Conference – AEC2020, Bordeaux, France, https://hal.archives-ouvertes.fr/hal-02859983, 2020.

Thanwerdas, J., Saunois, M., Berchet, A., Pison, I., Vaughn, B. H., Michel, S. E., and Bousquet, P.: Variational inverse modelling within the Community Inversion Framework to assimilate δ$^{13}C(CH_4)$ and CH_4: a case study with model LMDz-SACS, Geoscientific Model Development Discussions, pp. 1–29, https://doi.org/10.5194/gmd-2021-106, 2021.

Thompson, R. L., Nisbet, E. G., Pisso, I., Stohl, A., Blake, D., Dlugokencky, E. J., Helmig, D., and White, J. W. C.: Variability in Atmospheric Methane From Fossil Fuel and Microbial Sources Over the Last Three Decades, Geophysical Research Letters, 45, 11,499–11,508, https://doi.org/10.1029/2018GL078127, 2018.

Townsend-Small, A., Tyler, S. C., Pataki, D. E., Xu, X., and Christensen, L. E.: Isotopic measurements of atmospheric methane in Los Angeles, California, USA: Influence of "fugitive" fossil fuel emissions, Journal of Geophysical Research: Atmospheres, 117, https://doi.org/10.1029/2011JD016826, 2012.

Tyler, S. C., Crill, P. M., and Brailsford, G. W.: $^{13}C^{12}C$ Fractionation of methane during oxidation in a temperate forested soil, Geochimica et Cosmochimica Acta, 58, 1625–1633, https://doi.org/10.1016/0016-7037(94)90564-9, 1994.

van der Werf, G. R., Randerson, J. T., Giglio, L., van Leeuwen, T. T., Chen, Y., Rogers, B. M., Mu, M., van Marle, M. J. E., Morton, D. C., Collatz, G. J., Yokelson, R. J., and Kasibhatla, P. S.: Global fire emissions estimates during 1997–2016, Earth System Science Data, 9, 697–720, https://doi.org/10.5194/essd-9-697-2017, 2017.

Wang, X., Jacob, D. J., Eastham, S. D., Sulprizio, M. P., Zhu, L., Chen, Q., Alexander, B., Sherwen, T., Evans, M. J., Lee, B. H., Haskins, J. D., Lopez-Hilfiker, F. D., Thornton, J. A., Huey, G. L., and Liao, H.: The role of chlorine in global tropospheric chemistry, Atmospheric Chemistry and Physics, 19, 3981–4003, https://doi.org/10.5194/acp-19-3981-2019, 2019.

Wang, X., Jacob, D. J., Downs, W., Zhai, S., Zhu, L., Shah, V., Holmes, C. D., Sherwen, T., Alexander, B., Evans, M. J., Eastham, S. D., Neuman, J. A., Veres, P., Koenig, T. K., Volkamer, R., Huey, L. G., Bannan, T. J., Percival, C. J., Lee, B. H., and Thornton, J. A.: Global tropospheric halogen (Cl, Br, I) chemistry and its impact on oxidants, Atmospheric Chemistry and Physics Discussions, pp. 1–34, https://doi.org/10.5194/acp-2021-441, 2021.

Warwick, N. J., Cain, M. L., Fisher, R., France, J. L., Lowry, D., Michel, S. E., Nisbet, E. G., Vaughn, B. H., White, J. W. C., and Pyle, J. A.: Using delta^{13}C-CH_4 and deltaD-CH_4 to constrain Arctic methane emissions, Atmospheric Chemistry and Physics, 16, 14 891–14 908, https://doi.org/10.5194/acp-16-14891-2016, 2016.

Zazzeri, G., Lowry, D., Fisher, R. E., France, J. L., Lanoisellé, M., Kelly, B. F. J., Necki, J. M., Iverach, C. P., Ginty, E., Zimnoch, M., Jasek, A., and Nisbet, E. G.: Carbon isotopic signature of coal-derived methane emissions to the atmosphere:from coalification to alteration, Atmospheric Chemistry and Physics, 16, 13 669–13 680, https://doi.org/10.5194/acp-16-13669-2016, 2016.